Three-Dimensional Domain Identification in a Single Hexagonal Manganite Nanocrystal

Ahmed H. Mokhtar[1*], **David Serban**[1], **Daniel G. Porter**[3], **Frank Lichtenberg**[2], **Stephen P. Collins**[3], **Alessandro Bombardi**[3], **Nicola A. Spaldin**[2], **Marcus C. Newton**[1]

[1] School of Physics and Astronomy, University of Southampton
[2] Department of Materials, ETH Zurich
[3] Beamline I16, Diamond Light Source

Abstract

The three-dimensional domain structure in ferroelectric materials determines many of their physical and technological properties, including their electrostatic stability, coercive field and surface charge. The domain structure can be particularly complex in improper ferroelectrics such as the hexagonal manganites since the polarization is a slave to a non-ferroelectric primary order parameter that drives the domain formation. In antiferromagnetic $YMnO_3$, for example, this leads to an unusual hexagonal vortex domain pattern with topologically protected domain walls, which have been shown to exhibit electrical conductivity and a net magnetic dipole moment at the sample surface. Characterizing the three-dimensional structure of these domains and domain walls has been elusive, however, due to a lack of suitable imaging techniques.

Here, we present a multi-Bragg coherent x-ray diffraction imaging (BCDI) determination of the domain walls and domain types in a single $YMnO_3$ nanocrystal. By reconstructing high-resolution, three-dimensional images of the structure and the full strain tensor field, we resolve two ferroelectric domains separated by a domain wall and confirm that the primary atomic displacements occur along the crystallographic c-axis throughout the nanocrystal. By correlating the BCDI experiment with atomistic simulation, we are able to verify the "Mexican hat" symmetry model of domain formation in the hexagonal manganites, and establish that the two domains correspond to adjacent minima in the Mexican hat with opposite ferroelectric polarization and adjacent trimerization domains. Finally, using a circular mean comparison we show that for this sample the two domains correspond to a clockwise winding around the brim of the hat. Our results highlight the potential of multi-Bragg CDI combined with atomistic simulations for revealing and identifying ferroelectric domain structures.

Keywords: *Multiferroics; CDI; Phase-retrieval; Domains; Ferroelectricity; Topology*

1. Introduction

Ferroelectric materials have a spontaneous electric polarization that is switchable by the application of an electric field, making them useful in technological applications such as storage and transduction [1]. The switching proceeds via the motion of the domain walls separating domains of different polarization orientations, and a detailed description of the three-dimensional structure of the domains and domain walls is invaluable for optimizing the switching process, as well as for engineering domain walls as functional entities in their own right [2]. The domain structure in the class of improper multiferroic hexagonal manganites, $RMnO_3$ (R = Y, Sc or rare earth),

[*]**Corresponding author.** *E-mail address: ahmm1g15@soton.ac.uk*

is of particular interest since the improper nature of the ferroelectricity [3, 4] combines with the hexagonal symmetry to yield an unusual six-fold pattern of alternating polarization separated by topologically protected domain walls around string-like vortex cores [5]. These nanometer-sized topological defects, which can be controlled using electric fields, have been shown to exhibit electrical conductivity and magnetic properties, suggesting new pathways to novel devices such as mechanical sensors, transducers, and memories [6, 7]. The domain structure in the hexagonal manganites is formed on cooling through the symmetry-lowering structural phase transition (SPT) from the high symmetry paraelectric $P6_3/mmc$ phase to the ferroelectric $P6_3cm$ phase at high temperature; in the prototypical yttrium manganite, $YMnO_3$, this occurs at $T_c \sim 1250$K [8]. In the high symmetry structure, triangular planes of Y^{3+} ions separate planes of corner-shared MnO_5 trigonal bipyramids perpendicular to the crystallographic c axis, Figure 1a. The transition is driven by a unit-cell-tripling zone-boundary K_3 mode of the high-symmetry unit cell, which consists of a trimerizing tilting of the MnO_5 polyhedra accompanied by a buckling of the Y ions along the c direction, Figure 1b. Coupled with the K_3 mode is a polar Γ_2^- mode consisting of a uniform displacement of all Y ions in the same direction that causes an electric polarization along the c axis [9, 4]. The resulting energy surface resembles the iconic ϕ^4 Mexican hat potential, Figure 1d, but with six additional local minima in its brim at polyhedral tilting angles $\phi = \frac{n\pi}{3}$, corresponding to the six low-symmetry structural domains, often designated $\alpha+, \beta-, \gamma+, \alpha-, \beta+$ and $\gamma-$, where α, β and γ indicate three equivalent choices of origin for the tilting and $+, -$ indicate the polarization direction, Figure 1c [10].

Analogies have therefore been drawn between the domain formation process in the hexagonal manganites and other fundamental physical processes that are described by such a Mexican hat potential, with the hexagonal manganites proposed as a laboratory-based simulator for the formation of cosmic strings in the early universe [11, 12], as well as for aspects of Higgs-Goldstone physics [13, 14]. These fundamental and technological aspects clearly motivate a full three-dimensional mapping of the domain structure in the hexagonal manganites. Currently, however, this is lacking, with information about the sample interior inferred from microscopy [15] or scanning probe measurements [16] of the intersection of the domains with the surface, or from computer simulations.

In this paper, we image the domain structure of a YMO single nanocrystal by recovering the spatially resolved full strain tensor field using 3D Bragg coherent X-ray diffraction imaging (BCDI). BCDI is a particularly powerful tool for this purpose as it can reveal the ferroelectric domain structure in three dimensions as well as emerging crystal defects [17, 18]. BCDI is performed by illuminating a sample with a spatially coherent X-ray source so that the coherence length exceeds the dimensions of the crystal [19, 20]. Scattered light from the entire volume of the crystal interferes in the far field, producing a three-dimensional k-space diffraction pattern [21]. The experiment collects the 2D diffraction pattern of a selected reflection onto a detector while the 3^{rd} dimension is obtained by rocking the sample in increments and collecting the diffraction pattern at each step.

The Fourier space density and the real space electron density are related to each other by Fourier transforms, however, since the experiment only measures the intensity of the diffraction pattern, the phase information is lost as a result [22, 23]. Iterative phase retrieval methods like Hybrid Input-Output (HIO) algorithm are then used to recover the complex three-dimensional electron density and phase information [24, 25, 26, 27, 28]. The algorithm alternates between applying Fourier and real-space constraints on the electron density until it converges to a stable solution that satisfies the diffraction constraints.

The reconstructed real space phase information, $\phi(\mathbf{r})$, reveals a projection of the atomic displacement, $\mathbf{u}(\mathbf{r})$, at a point $\mathbf{r}$ in the crystal from equilibrium along the direction of the chosen $\mathbf{Q}$-vector in the experiment, according to $\phi(\mathbf{r}) = \mathbf{Q} \cdot \mathbf{u}(\mathbf{r})$. Hence, the real space phase enables the retrieval of atomic displacement parallel to the Bragg peak reciprocal lattice vector. The derivative of this displacement along the same vector provides the normal strain field, which serves as a proxy for identifying structural changes within the material. However, for a single Bragg peak, only a single projection of the displacement field is obtained. Consequently, components of the displacement field perpendicular to the scattering vector $\mathbf{Q}$ will not be observed in the BCDI measurement. To recover the full displacement field and strain tensor, diffraction patterns from multiple non-planar $\mathbf{Q}$-vector directions are required.

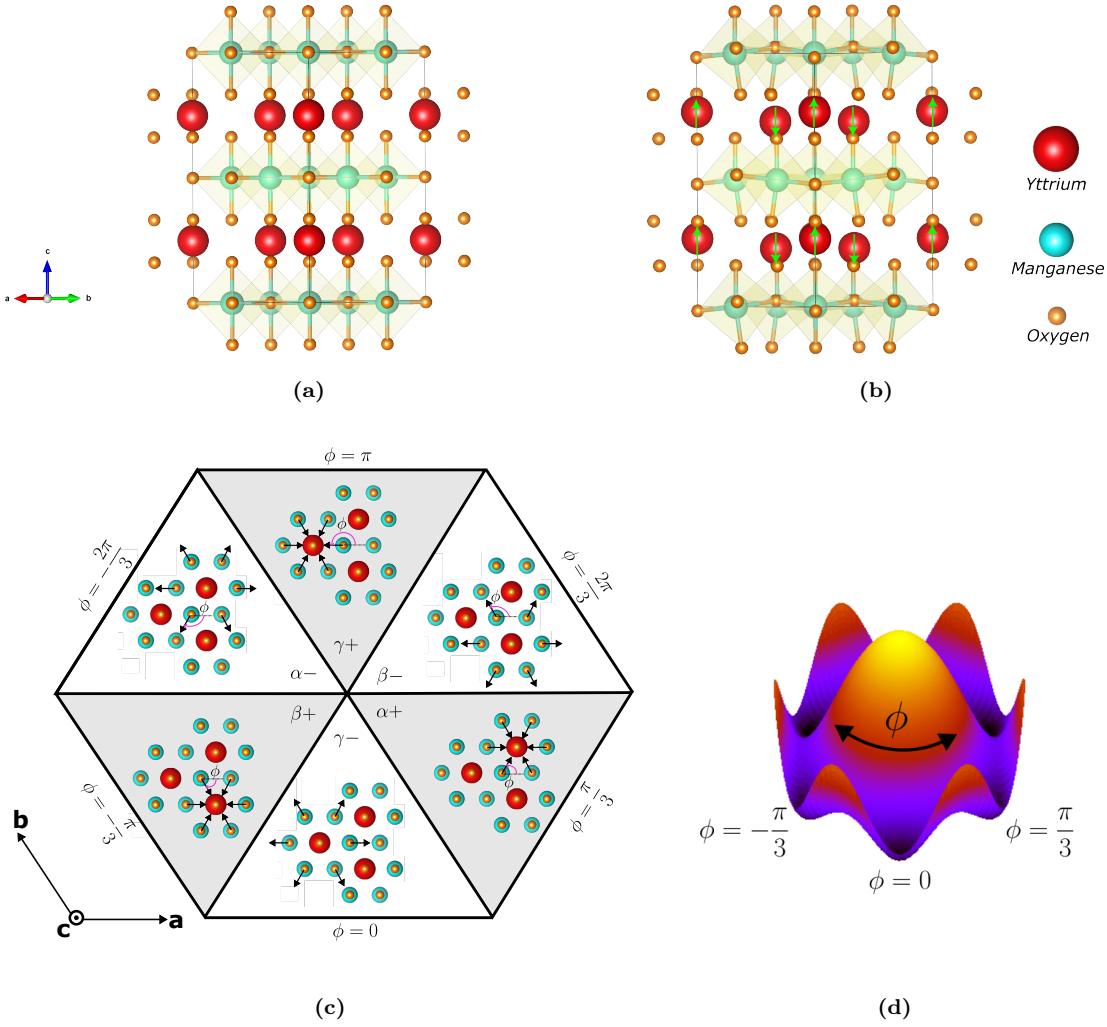

Figure 1. (a) & (b) Side-view of the paraelectric and ferroelectric unit cells, respectively. Y ions are in red, O ions in orange and Mn ions in green. The green arrows on the Y ions in (b) indicate the direction of displacements from the centrosymmetric phase. (c) Illustration of the six structural domains in $YMnO_3$ viewed down the c-axis, with the arrows indicating the displacements of the apical Oxygen ions which corresponds to the tilting of the MnO_5 polyhedra. (d) Potential energy surface of the $YMnO_3$ structural phase transition in $YMnO_3$. The energy of the centrosymmetric paraelectric state is at the peak of the hat. The six equivalent ferroelectric structures of (c) correspond to the six minima in the potential, with ϕ going around the hat.

2. Experimental Design

The experimental details of the preparation of the melt-grown crystalline YMO are reported in Reference [29]. Nanocrystals were then synthesized using a mixture of top-down and bottom-up approaches (see Methods section).

The BCDI experiment took place in air on beamline I16 at the Diamond Light Source synchrotron facility using x-rays of 9keV energy in the Bragg geometry on a 6-axis kappa diffractometer. The beam size was focused down to $200 \times 30\mu m$ with front slits set to $20 \times 20\mu m$. Multiple Bragg reflections from a single nanocrystal were located as described in the Methods section. Rocking curve measurements were performed on each reflection to obtain the three-dimensional diffraction patterns. In total, 5 specular reflections were identified, namely the (111), (110), (11$\bar{1}$), (212), and (300) reflections.

Conventional BCDI is typically performed on a single reflection. However, advancements in

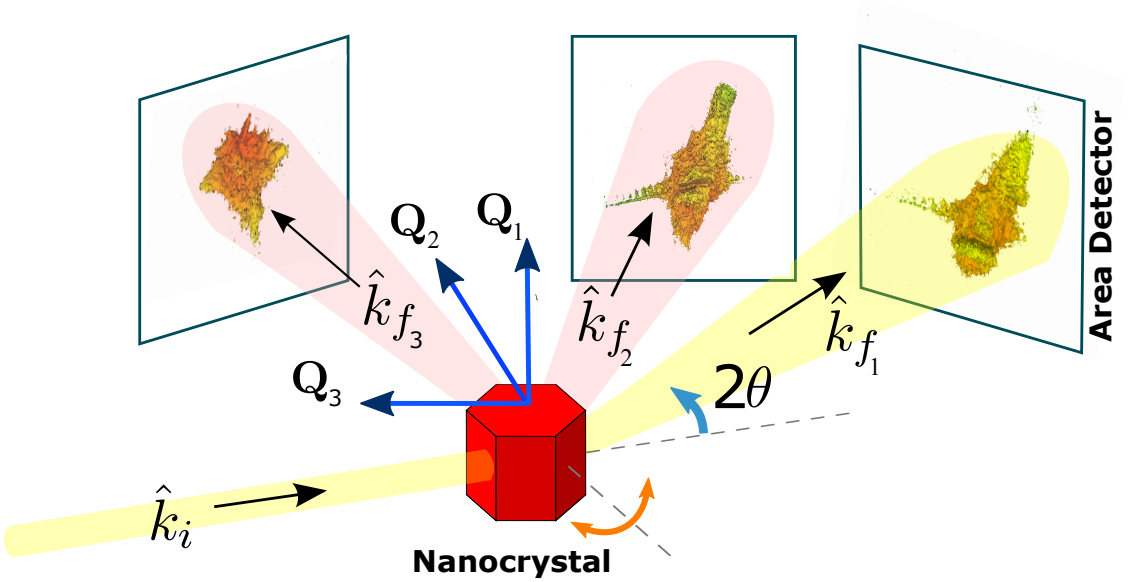

Figure 2. An illustration of the experimental geometry in a multi-Bragg CDI experiment. The 3 detector positions show real data taken in this experiment, from left to right: the (212), (111) and (110) diffraction data.

the field have facilitated the development of Multi-BCDI. This innovative approach allows for the concurrent analysis of multiple Bragg peaks from a single nanoparticle, thereby enabling the effective reconstruction of vector-valued lattice distortion fields within nanoscale crystals [30, 31, 32, 33].

Reconstructions of the full displacement field were performed concurrently using *The Interactive Phase Retrieval Suite* [34] as described in Ref. [30] by a combination of Fienup's HIO Mask [27] and Error Reduction [35] algorithms, with the support created using a manual version of the shrink wrap method. It accounts for geometric factors arising in BCDI measurements and allows for a globally constrained single image reconstruction to multiple Bragg peak measurements.

Additionally, our method involved an additional real space constraint based on the mean of the different amplitudes concurrently reconstructed from multiple Bragg reflections, since these reflections originated from the same crystal. This step was instrumental in accelerating the convergence of our phase retrieval process, enhancing the accuracy and efficiency of our reconstruction of the 3D strain field. During the reconstruction, it was realized that the diffraction patterns $(11\bar{1})$ and (300) reflections had very poor signal-to-noise ratios, hence, they were omitted from the reconstruction.

The other three patterns, displayed in Figure 2, contained sufficient information for the full reconstruction of the full strain tensor. The full reconstruction proceeded for $10,000$ iterations consisting of periodic cycles of HIO Mask and ER Mask algorithms in a $10:1$ ratio. Importantly, the requirement for extracting a full 3D strain tensor is not the orthogonality of these peaks, but their non-coplanarity. The non-coplanar arrangement of the three Bragg peaks in our experimental setup is a key factor that enables the effective extraction of the full 3D strain tensor.

Additionally, we observe that separate domains are encoded within the same diffraction pattern without separation in Fourier space which arises due to the uniformity of the c/a ratio across different domains. The distinguishing feature among these domains lies in the varied origins of rotation for the MnO_5 polyhedra. This aspect notably contrasts with other commonly studied ferroelectrics, where an anisotropic c/a ratio results in distinct pairs of Bragg reflections for each domain in reciprocal space [36]. Our atomistic simulations, discussed in subsequent sections of the paper, provide further corroboration of this characteristic in $YMnO_3$.

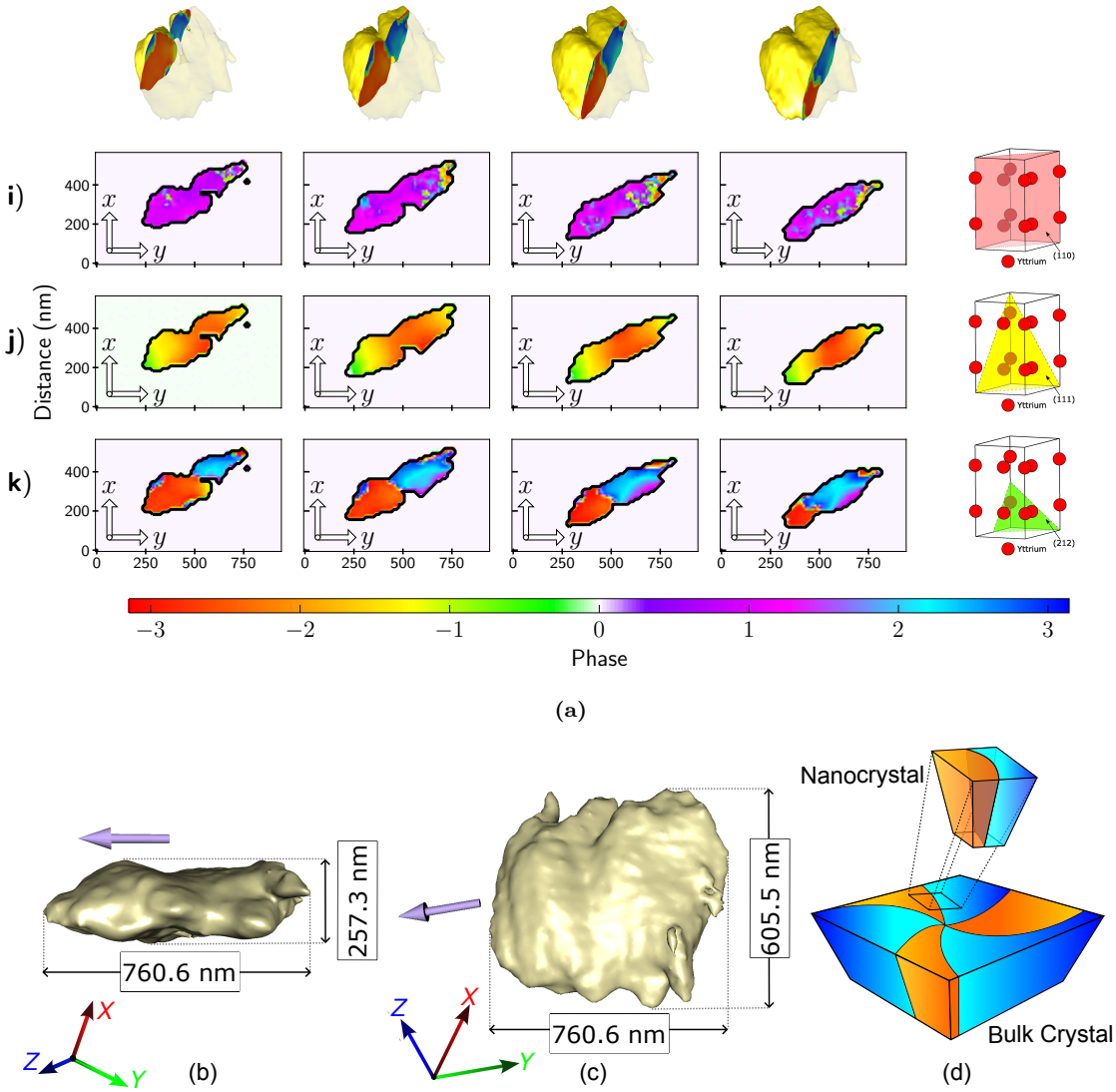

Figure 3. (a) 2D slices of the 3 reconstructed phase maps: i) the (111), j) (110) and k) (212) reflections. The red arrows are the propagation of the **q** vector onto the 2D plane for that particular reflection. The slices of the different phase maps are taken at the same angle (perpendicular to the x-axis) and at the same locations in the crystal. The 3D rendering of the crystal on the top row indicates the position at which the slices are taken. The last column illustrates the different planes for each of the reflections and displays the Yttrium ions' positions in the unit cell. (b) & (c) 3D renderings of the reconstructed crystal taken from two different viewpoints at 70% of amplitude. The (212) **Q**-vector displayed in purple. (d) An illustration of how the two observed domains form part of the 6 intersecting domains in the bulk crystal.

3. Results and Discussion

The precision in our diffraction measurements is underscored by the close match between the observed 2θ values and their calculated counterparts for the studied reflections using the reported lattice parameters [37]. This match is quantitatively expressed by the quantity $\sum \frac{|2\theta_{\text{obs}} - 2\theta_{\text{calc}}|}{2\theta_{\text{calc}}} < 10^{-3}$ indicating an exceptionally high level of accuracy. This correspondence not only confirms the accuracy of our measurements but also validates the correct phase and stoichiometry of the

material.

We also investigated the fringe frequency in our diffraction patterns to confirm that all patterns originated from the same crystal. Given the random size and morphology of nanocrystals on the substrate, we needed to ensure the fringe frequencies across the diffraction patterns were consistent. To this end, we performed a line scan in the same direction for all five diffraction patterns and computed the Fourier transform of these scans to determine the frequency. The results were strikingly similar, with frequencies centered around 250 nm, Figure S2 of the Supplementary Material. Thereby confirming that the patterns originated from the same crystal as the likelihood of two crystals having identical orientation matrices and sizes in a randomly distributed sample is exceedingly low. The calculated fringe frequency matches one of the reconstructed crystal's dimensions, as expected, providing further validation that the diffraction patterns originate from the same crystal.

The 3D reconstruction of the electron density, Figures 3b and 3c, reveals the dimensions of the crystal to be $761 \times 605 \times 257$ nm^3, with a 13 nm resolution which includes the $5-10$ nm layer added by PLD. The orientation of the c-axis was determined using the known directions of the **Q**-vectors and the geometry of the unit cell. For simplicity in data interpretation, we then rotated the crystal such that its c-axis aligned with the z-axis.

Sliced planes were then taken at different positions along the crystal, perpendicular to the z-axis, to obtain phase maps for each of the reflections; Figure 3a shows slices of the x-y plane. The full phase map is presented in the supplementary material. The added layer by PLD does not manifest itself in the phase information nor does it influence the domain structure observed or the overall phase of the material, hence, it can be neglected.

The phase map along (212) reveals the existence of two domains with high phase values and hence large displacement along that **Q** vector direction. Domain 1 exhibits a mean phase value of 2.25 ± 0.006rad , while Domain 2 has a mean phase value of -2.54 ± 0.004rad. The near symmetry in the phase values and their low standard error indicate similar magnitudes of lattice distortions in opposite directions. This is characteristic of a domain boundary rather than dislocation-induced lattice distortion.

In contrast, the phase information of dislocations would manifest as localized disruptions in the crystal lattice and a gradual phase change away from the dislocation site due to lattice relaxation [38, 39]. The phase changes observed here are step-like, with each domain exhibiting a low standard error which is indicative of a small phase gradient.

Additionally, in our work, the phase contrast is predominantly visible in the (212) direction, and notably absent in the (110) and (111) phase maps. This selective visibility supports the interpretation that (212) contrasts are indicative of domain boundaries rather than dislocations, as a dislocation would likely be visible in the other phase maps. Additionally, the selective visibility is consistent with our atomistic simulations discussed later in the paper.

Furthermore, the crystal shows no obvious signs of Oxygen depletion at the surface when scaled down to the nanoscale. The absence of Oxygen diffusion is consistent with the bulk material. Typically, Oxygen depletion would manifest as a distinct phase at the crystal's surface, but this is not observed in our results, further supporting the integrity of our material preparation.

The locations and widths of these (212) boundaries differ from those observed for the (110) reflection reflecting their distinct origins. The structure along the (110) axis reveals a domain boundary made up of phases equal to zero, implying that there is no displacement along that direction in this region along that direction. The neighboring domains exhibit low phase values, indicating just a minor displacement. This aligns with expectations, as the Yttrium ion displacement occurs along the crystal's c-axis, and the (110) Q-Vector does not have a component in that direction. Consequently, the (110) phase map is reflective of displacements in the crystal's ab-plane likely caused by some small crystal imperfections or secondary strain effects.

In the (111) phase map, no distinction between the domains was observed in the (111) phase map despite the **Q**-vector having a component along the c-axis. This lack of distinction can be attributed to the symmetry of Yttrium ion displacement around (111) **Q**-vector direction, which

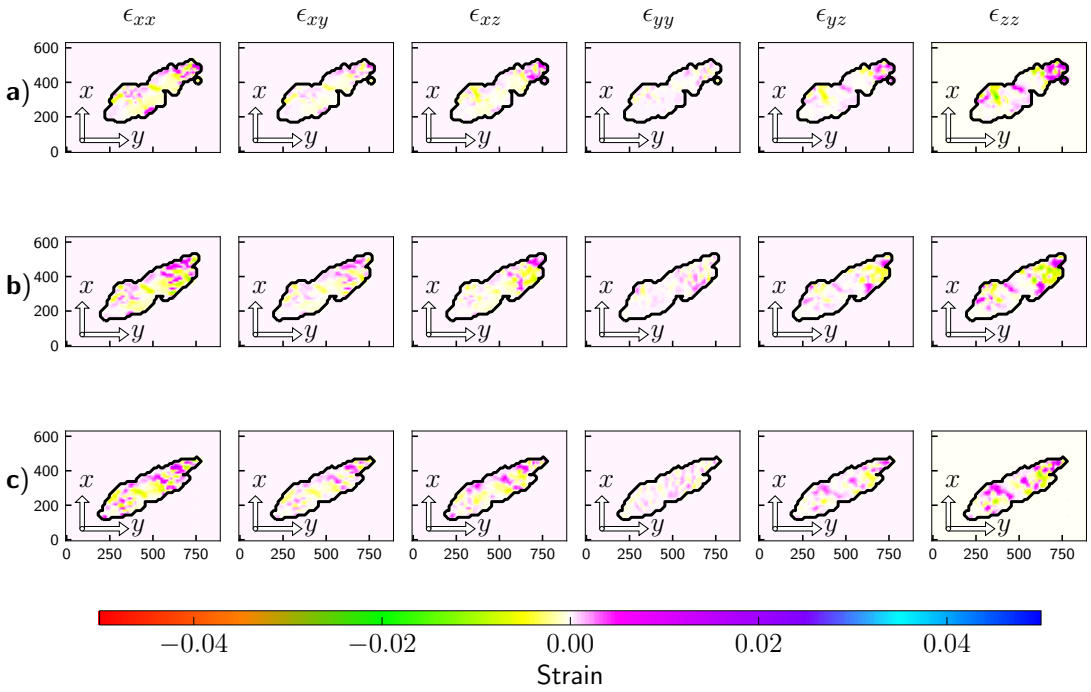

Figure 4. The reconstructed strain tensor of the crystal, computed as described in the text. The 6 columns represent each of the 6 independent components of the strain tensor. Each row is a slice in the crystal taken at three of the four planes in Figure 3a

effectively masks the differentiation between domains in the (111) phase map. This observation is corroborated by the atomistic simulations discussed later in the paper, which further illustrate the symmetrical nature of these displacements when projected onto that direction.

To further confirm the origin of these domains we computed the strain tensor field in the crystal. The strain tensor was computed from the reconstructed displacement field according to Equation 1,

$$\epsilon_{ij} = \frac{1}{2}\left(\frac{\partial \mathbf{u}_i}{\partial x_j} + \frac{\partial \mathbf{u}_j}{\partial x_i}\right) \tag{1}$$

where ϵ represents the strain tensor, and subscripts i, j indicate the different components of the tensor. Figure 4 displays slices of the 6 independent components of the strain tensor taken at three of the four planes presented in Figure 3a. The full strain tensor field is presented in the Supplementary information.

The domain wall is most evident in the ϵ_{zz} and ϵ_{yz} components as illustrated in Figures 4. It is marked by distinct purple strings and is notably absent in the ϵ_{xx} and ϵ_{yy} components. The strings align with the domain wall identified in the (212) phase map, highlighting the displacement direction between different domains. The c-axis vector aligns with the z-axis which suggests that the observed displacement between domains is primarily due to Yttrium ion movement along the c-axis. In the strain tensor, dislocations typically exhibit circular wraps and a profile of gradual increase or decrease. Therefore, the observed profile further supports the existence of ferroelectric domains.

Piezoforce microscopy (PFM) images of the bulk crystal in Reference [29] reveal the density of vortex cores at the surface to be $0.3\frac{\text{cores}}{\mu m^2}$. Given this vortex density and the small size of the crystal, observation of a complete vortex or multiple vortices is improbable. Therefore, we are observing a small portion of the full structure, a section that contains two domains separated by a domain wall as illustrated in Figure 3d.

Our investigations reveal that the vortex structure within the crystal is independent of the crystal's size as the topological structures remain unaffected by variations in the crystal's dimensions. Notably, the stability and consistency of the vortex size, irrespective of the crystal size, align with theoretical expectations. Such behavior underscores the topological protection inherent in these structures, suggesting that their characteristics are fundamentally governed by topological constraints rather than geometrical dimensions of the crystal.

Our focus is primarily on the order parameter of the different domains exhibited in the (212) phase map and the direction of its change, which we have determined to be along the c-axis. Using this information, the domain types in the (212) phase can be determined using an atomistic simulation of BCDI 3D diffraction patterns with lattice distortions as described in the Methods section. We consider the Yttrium and planar Oxygen ions' displacements along the c-axis in the 6 domains relative to their positions in the centrosymmetric paraelectric phase. This choice is supported by the strain field information that indicates the major displacement between the domain occurs along that direction. An arbitrary choice of origin is selected and fixed for all the simulated domains while the ions are displaced differently in each of the domains, leading to an overall change in the momentum transfer vector along certain **Q**-vector directions. The displacement values were extracted from [37], with the Yttrium ions' movements for the choice of origin illustrated in Figure 5b and the planar Oxygen ions are made to displace in the opposite directions; as described in Ref. [40] and Ref. [41].

The 3D diffraction pattern was simulated for the three experimental reflections and the real space phase information was obtained. Figure 5a displays the phase information in each of the domains for each reflection. The (212) reflection exhibited distinguished phase information between different domains, with variations in the phase difference between the neighboring domains. This information can be used to compare the difference between the neighboring domains in the simulated crystal with the difference between the two observed experimental domains. To account for the periodic nature of the phase, the differences between domains were characterized by computing the circular variance (Equation 2),

$$Var(\phi) = \arctan\left(\frac{\sin(\phi_i - \phi_j)}{\cos(\phi_i - \phi_j)}\right). \tag{2}$$

Within each domain in the simulated data, the phase value is constant, however, in the experimental results, a mean value was computed for each domain. Figure 5c displays the result from these computations clearly showing a close match of the experimental and simulated circular mean at the $\gamma-, \beta+$ and $\alpha+, \gamma-$, regions with a χ^2 of 0.007 and 0.071, respectively. This signifies that the $\gamma-, \beta+$ forms a better fit with a χ^2 value that is an order of magnitude lower. It can then be determined that the two observed domains in the (212) phase map are $\beta+$ and $\gamma-$ for the positive and negative phase regions, respectively, as they form better alignment with the theoretical model.

The circular mean is a non-commutative quantity, hence, its polarity has some significance in determining the vortex direction. The circular mean values in figure 5c for the simulated results were computed with an anti-vortex order, hence, a matched polarity with the experimental results is indicative that the two domains observed are part of an anti-vortex structure in this case, i.e. a clockwise movement around the brim of the Mexican-hat potential as illustrated in Figure 5d.

As expected, the simulated phase in the (110) reflection was zero throughout the whole crystal as only the displacement along the crystal's c-axis was considered. The simulated results of the (111) reflection demonstrated a constant non-zero phase in the whole crystal, i.e. the domains are indistinguishable from each other along that direction. It can be said that the projection of the Yttrium ions' displacements along that **Q**-vector direction poses symmetry that detects the displacements but does not distinguish them from each other. This result is consistent with the experimental result for the (111) phase map as we observe, although not strictly uniform, a non-zero phase in addition to the domains being indistinguishable from each other. The absence of the domain primary order parameter within the experimental and the simulated results highlights the aforementioned symmetry and the reliability of our method.

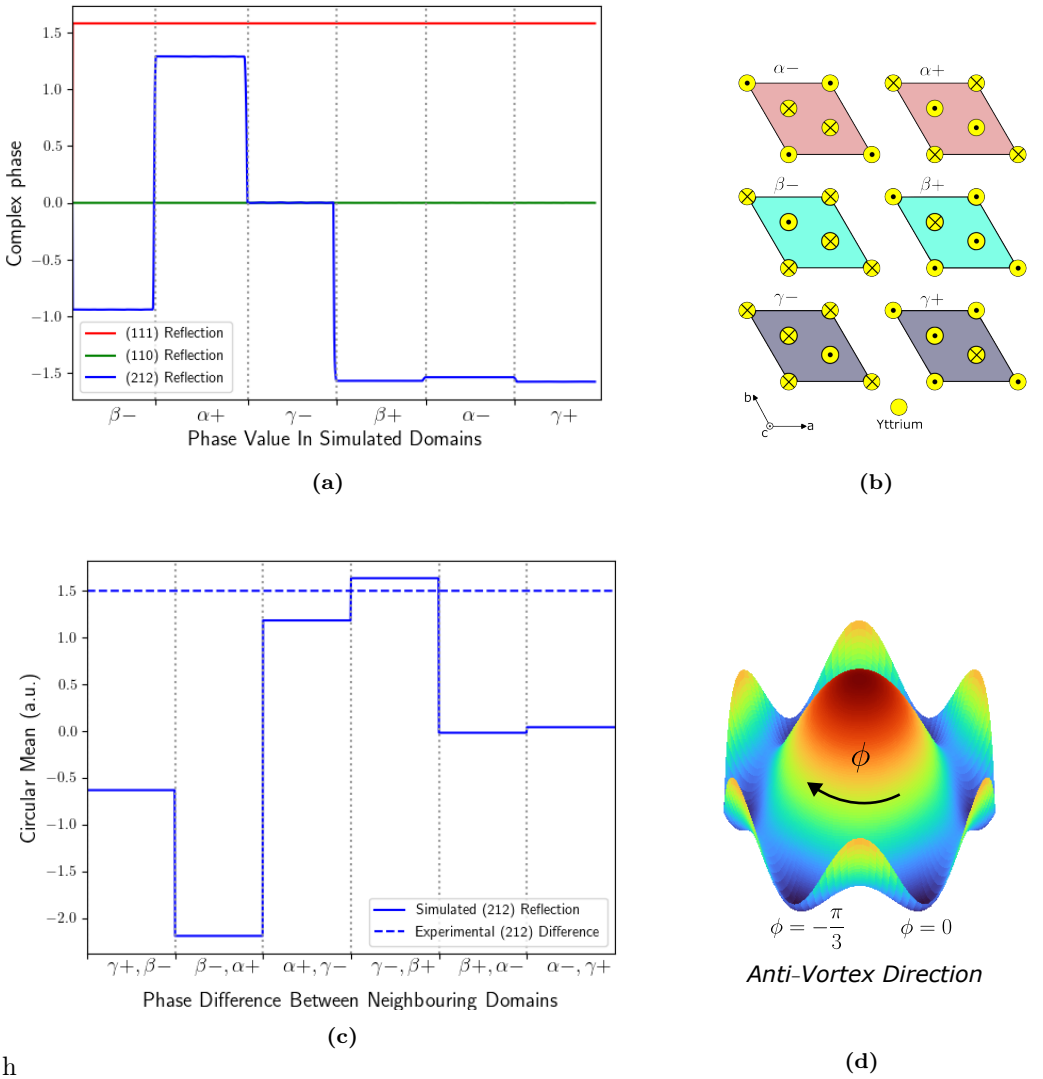

h

Figure 5. (a) A plot of the scan through the simulated crystal showing the different domains. (c) A plot of the calculated circular variance between the phase of neighboring domains for the simulated (colored solid lines) and experimental (colored dotted line). The black vertical dotted lines separate the different regions as indicated in the figure. A match between the simulated and experimental values for the (212) reflection at the $\beta+$ and $\gamma-$ region concludes the type of domains observed experimentally. (b) Illustrations of the ions' movements in the ferroelectric unit cell relative to their positions in the paraelectric phase for the Yttrium ions. (d) The clockwise arrow indicates an anti-vortex structure as is the case for the observed crystal.

4. Conclusion

In conclusion, we report a multi-Bragg CDI experiment on a single YMO nanocrystal and demonstrate the success of the concurrent phase retrieval algorithm. In addition, we identified a method of determining ferroelectric domain types from the reconstructed phase information. Phase maps for each of the three reflections along with the strain tensor field detail the behavior of the material.

The (212) phase map revealed two separate ferroelectric domains forming in the crystal. The two domains were identified as $\gamma-$ and $\beta+$ for our choice of origin by comparison with simulated results of the domains' structure for that reflection. We were also able to identify the two domains

to be a part of an anti-vortex structure. Small displacements were observed in the (110) phase map which was attributed to crystal defects as there are no displacements of the Yttrium ions along that direction. No obvious surface defects such as Oxygen depletion or a structural change due to a depolarization field were observed in any of the phase maps.

The ability to image and identify ferroelectric domains in a single YMO nanocrystal can facilitate the design and characterization of devices formed from YMO where domains play a pivotal role. Our finds are therefore of considerable utility for the development of next-generation technologies based on multiferroic hexagonal manganite materials.

5. Methods

5.1. Synthesis of YMO Nanocrystals

Nanocrystals of YMO were synthesized as follows. By means of mechanical grinding and ultrasonication of a small piece of the melt-grown sample, a low-density nano-powder solution was formed and deposited on a bare Si (100) substrate followed by dispersion using a spin-coater to obtain an even distribution over the surface. The nano-powder acted as seeds for a pulsed laser deposition (PLD) operation aiming to correct surface imperfections caused by the grinding process and sufficient adhesion of the nanocrystal to the substrate. PLD took place in an ultra-high vacuum condition in the presence of Argon; an excimer laser was used to ablate the melt-grown YMO sample forming a plasma. This is then directed on the substrate where the material condenses at the seed sites in a stoichiometric manner. The PLD process was run for only 16 cycles at 5Hz and 600° such that only $5-10$ nm of material is deposited. The sample was then gently annealed at 600°C for 6 hours to relax any strain present.

5.2. Locating Multiple Bragg Reflections

The detector employed in our experiments was the Quad Merlin detector, featuring 515×515 pixels, with each pixel measuring $55\mu m \times 55\mu m$. The sample-to-detector distance during measurements was 1.31 meters. The full beam x-ray flux at the sample is 3×10^{13} photons/s with a beam size of $200\mu m(h) \times 30\mu m(v)$, for these measurements we employed slits before the sample with size $20\mu m \times 20\mu m$, reducing the beam size and used Al foils to attenuate the incident flux by 70% to mitigate beam damage to the sample.

Using surface area scans, a single nanocrystal was identified at the (111) specular reflection and was positioned at the eucentric point. Using this as the primary reflection, other reflections were found by measuring the cone about the primary reflection using the inter-planar angle. Reflections were identified as being from the same grain if the inter-planar angle agreed and the peaks had the same profile. Two reflections are enough to define an orientation matrix, which was then used to find further reflections using the DiffCalc software [42].

5.3. Simulation of BCDI Diffraction Patterns

The simulation considers the displacements of individual atoms from their equilibrium position and computes the scattering amplitude according to Equation 3,[19]

$$\begin{aligned} A(\mathbf{q}) &= \frac{r_0\sqrt{\phi_0}}{R}\sum_{\mathbf{R}_n}\sum_{\mathbf{r}_m}\mathcal{F}_m(\mathbf{q})e^{-i\mathbf{q}\cdot(\mathbf{R}_n^m+\mathbf{u}_m(\mathbf{R}_n))} \\ &\approx \frac{r_0\sqrt{\phi_0}}{R}\prod_i d_i\sum_{\mathbf{R}_{nd}}\sum_{\mathbf{r}_m}\mathcal{F}_m(\mathbf{q})e^{-i\mathbf{q}\cdot(\mathbf{R}_{nd}^m+\tilde{\mathbf{u}}_m(\mathbf{R}_{nd}))} \end{aligned} \tag{3}$$

where r_0 is the Thompson scattering factor, $\mathcal{F}_m(\mathbf{q})$ is the atomic form factor, $\mathbf{u}_m$ is the displacement of atom m from equilibrium, $\mathbf{R}_n$ are unit cell vectors and $\mathbf{r}_m$ are fractional coordinates of atom m in the unit cell. The computationally expensive problem of summing over all atoms is simplified by considering the summation over groups of adjacent unit cells as shown in the second line of Equation 3; where $\mathbf{R}_{nd}^m = \mathbf{R}_{nd} + \mathbf{r}_m$, $\mathbf{R}_{nd} = n_1d_1\mathbf{a}_1 + n_2d_2\mathbf{a}_2 + n_3d_3\mathbf{a}_3$ and $\tilde{\mathbf{u}}_m$ is the average displacement of atom m at position $\mathbf{R}_{nd}$.

6. Acknowledgement

This work was supported by UK Research and Innovation (UKRI) grant MR/T019638/1 for the University of Southampton Department of Physics & Astronomy. The authors acknowledge the use of the IRIDIS High-Performance Computing Facility, and associated support services at the University of Southampton, in the completion of this work. We acknowledge Diamond Light Source for time on Beamline I16 under Proposal MM30073-1.

7. Data Availability

The data underpinning the findings of this study are available from M.C.N upon reasonable request.

8. Code Availability

The computational analysis in this study utilized two distinct codebases. The code for the concurrent phase retrieval algorithm is part of "Bonsu: The Interactive Phase Retrieval Suite" software package, and can be downloaded through PyPI (https://pypi.org/project/Bonsu/) or GitHub (https://github.com/bonsudev/bonsu). Additionally, the code used for the simulations conducted in this study is available within the DiffSim package through PyPI (https://pypi.org/project/diffsim/) or GitHub (https://github.com/bonsudev/diffsim).

Both are integral to the research and are made available to ensure transparency and reproducibility in scientific research. The provided links offer direct access to the respective code repositories, enabling other researchers to utilize and build upon the computational work conducted in this study.

References

[1] K. M. Rabe, C. H. Ahn, and J.-M. Triscone, *Physics of Ferroelectrics*. Springer Berlin, Heidelberg, 2007.

[2] D. Meier, J. Seidel, M. Gregg, and R. Ramesh, *Domain Walls: From Fundamental Properties to Nanotechnology Concepts*. Oxford University Press, 2000.

[3] B. B. van Aken, T. T. M. Palstra, A. Filippetti, and N. A. Spaldin, "The origin of ferroelectricity in magnetoelectric $YMnO_3$," *Nat. Mater.*, vol. 3, pp. 164–170, 2004.

[4] C. J. Fennie and K. M. Rabe, "Ferroelectric transition in $YMnO_3$ from first principles," *Phys. Rev. B*, vol. 72, p. 100103(R), 2005.

[5] S. C. Chae, Y. Horibe, D. Y. Jeong, S. Rodan, N. Lee, and S.-W. Cheong, "Self-organization, condensation, and annihilation of topological vortices and antivortices in a multiferroic," *Proceedings of the National Academy of Sciences of the United States of America*, vol. 107, no. 50, pp. 21 366–21 370, 2010.

[6] D. Meier and S. M. Selbach, " Ferroelectric domain walls for nanotechnology," *Nat. Rev. Mater.*, vol. 7, p. 157–173, 2022.

[7] P. Sharma, P. Schoenherr, and J. Seidel, "Functional ferroic domain walls for nanoelectronics," *Materials*, vol. 12, p. 2927, 09 2019.

[8] S. C. Abrahams, "Ferroelectricity and structure in the $YMnO_3$ family," *Acta Crystallogr. B*, vol. 57, no. 4, pp. 485–490, Aug. 2001.

[9] T. Lonkai, D. G. Tomuta, U. Amann, J. Ihringer, R. W. A. Hendrikx, D. M. Tobbens, and J. A. Mydosh, "Development of the high temperature phase of hexagonal manganites," *Phys. Rev. B*, vol. 69, p. 134108, 2004.

[10] S. Artyukhin, K. T. Delaney, N. A. Spaldin, and M. Mostovoy, "Landau theory of topological defects in multiferroic hexagonal manganites," *Nat. Mater.*, vol. 13, pp. 42–49, 2014.

[11] T. W. B. Kibble, "Topology of cosmic domains and strings," *Journal of Physics A: Mathematical and General*, vol. 9, no. 8, pp. 1387–1398, aug 1976.

[12] S. M. Griffin, M. Lilienblum, K. T. Delaney, Y. Kumagai, M. Fiebig, and N. A. Spaldin, "Scaling behavior and beyond equilibrium in the hexagonal manganites," *Phys. Rev. X*, vol. 2, p. 041022, 2012.

[13] P. W. Higgs, "Broken symmetries and the masses of gauge bosons," *Phys. Rev. Lett.*, vol. 13, pp. 508–509, Oct 1964.

[14] Q. Meier, A. Stucky, J. Teyssier, S. Griffin, D. van der Marel, and N. A. Spaldin, "Do indications of crystallographic Higgs and Goldstone dynamics manifest in the hexagonal manganites?" 2019, in preparation.

[15] T. Choi, Y. Horibe, H. T. Yi, Y. J. Choi, W. Wu, and S.-W. Cheong, "Insulating interlocked ferroelectric and structural antiphase domain walls in multiferroic $YMnO_3$," *Nat. Mater.*, vol. 9, pp. 253–258, 2010.

[16] T. Jungk, Á. Hoffmann, M. Fiebig, and E. Soergel, "Electrostatic topology of ferroelectric domains in $YMnO_3$," *Appl. Phys. Lett.*, vol. 97, p. 012904, 2010.

[17] J. Miao, T. Ishikawa, I. Robinson, and M. M. Murnane, "Beyond crystallography: Diffractive imaging using coherent x-ray light sources," *Science*, vol. 348, pp. 530–535, 2015.

[18] J. Miao, D. Sayre, and H. N. Chapman, "Phase retrieval from the magnitude of the fourier transforms of nonperiodic objects," *J. Opt. Soc. Am. A*, vol. 15, no. 6, pp. 1662–1669, Jun 1998.

[19] A. H. Mokhtar, D. Serban, and M. C. Newton, "Simulation of bragg coherent diffraction imaging," *Journal of Physics Communications*, vol. 6, no. 5, p. 055003, may 2022.

[20] I. Robinson and R. Harder, "Coherent x-ray diffraction imaging of strain at the nanoscale," *Nature materials*, vol. 8, pp. 291–8, 05 2009.

[21] J. Miao, J. Kirz, and D. Sayre, "The oversampling phasing method," *Acta Crystallographica Section D*, vol. 56, no. 10, pp. 1312–1315, Oct 2000.

[22] M. C. Newton, R. Harder, X. Huang, G. Xiong, and I. K. Robinson, "Phase retrieval of diffraction from highly strained crystals," *Phys. Rev. B*, vol. 82, p. 165436, Oct 2010.

[23] M. C. Newton, A. D. Parsons, U. Wagner, and C. Rau, "Coherent x-ray diffraction imaging of photo-induced structural changes in bifeo3 nanocrystals," *New Journal of Physics*, vol. 18, 2016.

[24] M. Newton, S. Leake, R. Harder, and I. Robinson, "Three-dimensional imaging of strain in a single zno nanorod," *Nature Materials*, vol. 9, pp. 120–124, 2009.

[25] J. R. Fienup, "Reconstruction of an object from the modulus of its fourier transform," *Opt. Lett.*, vol. 3, no. 1, pp. 27–29, Jul 1978.

[26] H. H. Bauschke, P. L. Combettes, and D. R. Luke, "Phase retrieval, error reduction algorithm, and fienup variants: a view from convex optimization," *J. Opt. Soc. Am. A*, vol. 19, no. 7, pp. 1334–1345, Jul 2002.

[27] J. R. Fienup, "Phase retrieval algorithms: a comparison," *Appl. Opt.*, vol. 21, no. 15, pp. 2758–2769, Aug 1982.

[28] S. Marchesini, "Invited article: A unified evaluation of iterative projection algorithms for phase retrieval," *Review of Scientific Instruments*, vol. 78, no. 1, p. 011301, 2007.

[29] F. Lichtenberg, M. Lilienblum, B. Batlogg, N. Spaldin, and M. Fiebig, "Synthesis of melt-grown hexagonal $YMnO_3$, $YMn_{0.95}O_{2.93}$, $YMnO_{3+y}$, and $DyMnO_{3-d}$ and study of their properties by powder x-ray diffraction, piezoresponse force microscopy, a SQUID magnetometer, and thermogravimetry," Report, publication of research results in form of a presentation by the library of the ETH Zurich / ETH Research Collection, 2019.

[30] M. C. Newton, "Concurrent phase retrieval for imaging strain in nanocrystals," *Phys. Rev. B*, vol. 102, p. 014104, Jul 2020.

[31] M. J. Wilkin, S. Maddali, S. O. Hruszkewycz, A. Pateras, R. L. Sandberg, R. Harder, W. Cha, R. M. Suter, and A. D. Rollett, "Experimental demonstration of coupled multi-peak bragg coherent diffraction imaging with genetic algorithms," *Phys. Rev. B*, vol. 103, p. 214103, Jun 2021.

[32] Y. Gao, X. Huang, H. Yan, and G. J. Williams, "Bragg coherent diffraction imaging by simultaneous reconstruction of multiple diffraction peaks," *Phys. Rev. B*, vol. 103, p. 014102, Jan 2021.

[33] S. Maddali, T. Frazer, N. Delegan, K. Harmon, S. Sullivan, M. Allain, W. Cha, A. Dibos, I. Poudyal, S. Kandel, Y. Nashed, F. J. Heremans, H. You, Y. Cao, and S. Hruszkewycz, "Concurrent multi-peak bragg coherent x-ray diffraction imaging of 3d nanocrystal lattice displacement via global optimization," vol. 9, 06 2023.

[34] M. Newton, Y. Nishino, and I. Robinson, "Bonsu: The interactive phase retrieval suite," *Journal of Applied Crystallography*, vol. 45, 08 2012.

[35] J. R. Fienup, "Reconstruction of a complex-valued object from the modulus of its fourier transform using a support constraint," *J. Opt. Soc. Am. A*, vol. 4, no. 1, pp. 118–123, Jan 1987.

[36] J. Diao, X. Shi, T. A. Assefa, L. Wu, A. F. Suzana, D. S. Nunes, D. Batey, S. Cipiccia, C. Rau, R. J. Harder, W. Cha, and I. K. Robinson, "Evolution of ferroelastic domain walls during phase transitions in barium titanate nanoparticles," *Phys. Rev. Mater.*, vol. 4, p. 106001, Oct 2020.

[37] S. C. Abrahams, "Atomic displacements at and order of all phase transitions in multiferroic $YMnO_3$ and $BaTiO_3$," *Acta Crystallographica Section B*, vol. 65, no. 4, pp. 450–457, Aug 2009.

[38] M. J. Cherukara, R. Pokharel, T. S. O'Leary, J. K. Baldwin, E. Maxey, W. Cha, J. Maser, R. J. Harder, S. J. Fensin, and R. L. Sandberg, "Three-dimensional x-ray diffraction imaging of dislocations in polycrystalline metals under tensile loading," *Nature Communications*, vol. 9, no. 1, p. 3776, 2018.

[39] A. Ulvestad, Y. Nashed, G. Beutier, M. Verdier, S. O. Hruszkewycz, and M. Dupraz, "Identifying defects with guided algorithms in bragg coherent diffractive imaging," *Scientific Reports*, vol. 7, no. 1, p. 9920, 2017.

[40] Q. Zhang, G. Tan, L. Gu, Y. Yao, C. Jin, Y. Wang, X. Duan, and R. C. Yu, "Direct observation of multiferroic vortex domains in $YMnO_3$," *Scientific reports*, vol. 3, p. 2741, 09 2013.

[41] B. Van Aken, T. Palstra, A. Filippetti, and N. Spaldin, "The origin of ferroelectricity in magnetoelectric $ymno_3$," *Nature materials*, vol. 3, pp. 164–70, 2004.

[42] R. Walton, "DiffCalc: A diffraction condition calculator for X-ray or neutron diffractometer control."